The Structure of Some Variable-Density Shear Flows

Laurent Joly
Department of Fluid Mechanics, ENSICA
1, Place Emile Blouin, 31056 Toulouse Cedex, France
laurent@ensica.fr

Preamble

The following discussion focuses on the influence of density contrasts on the development of basic shear flows. It is expected, as usual, that what is learnt from these prototype flows can be transposed, at least locally, to more complex geometries. The specific features of these variable-density flows are best accounted for as seen from their vorticity dynamics. The baroclinic torque, connecting misaligned pressure and density gradients, reorganizes the vorticity field according to the fluid inertia. It gives rise to thinner vorticity patches thus shifting enstrophy toward higher wave numbers. It also changes the stability characteristics and the transition to turbulence of laminar shear flows. While frequently commented in geophysical flows under the Boussinesq approximation, it nonetheless deserves a particular attention in the context of inertia-dominated flows encountered in high Reynolds number mixing situations.

The baroclinic torque is introduced after a short literature survey. Then the particular cases of the mixing layer and the jet are examined. The two-dimensional and some three-dimensional aspects are documented based on temporally and spatially developing numerical simulations.

This paper has directly benefitted from the results obtained by J. Reinaud during his PhD thesis and from discussions with V. Chapin, P. Chassaing and J. Micallef, whom I warmly thank.

Contents

1 Introduction

In the paper of Brown & Roshko (1974), often cited because of its striking spark shadow pictures of coherent structures, one can find a clear introduction to the questions risen at that time upon density and compressiblity effects on the self-preserving development of turbulent mixing layers. The main concern was then on the alteration of their downstream spreading rate. That paper demonstrated that the density ratio between the two streams had a significant influence on the spreading rate even if milder than the drastic reduction resulting from increasing Mach numbers. It was followed by numerous studies of fully turbulent compressible mixing-layers connected with new proposals for the turbulence closure-schemes in the compressible context, see the succesful attempts by Sarkar (1992) or Zeman (1990) and the comprehensive review by S.K.Lele (1994). The later studies of Vreman, Sandham & Luo (1996) and Sarkar & Pantano (2000) have benefitted from the direct numerical simulations and pointed toward the reduction of pressure fluctuations and the shifting of the maximum Reynolds stress towards the lighter stream. These studies, motivated by a renewied interest in high speed civil aircraft propulsion, focused on the fully turbulent statistical prediction of the shear layer. The density ratio and the connected mean and fluctuating inertia effects were merely considered as resulting from the upstream supersonic conditions.

Other industrial applications in low-speed combustion and mixing are nevertheless demanding the analysis and prediction of inertia effects alone. Provided these findings are uncorrelated to compressibility, this may also provide a simpler context to elucidate the density ratio effect and transpose the conclusions to compressible flows. This approach is clearly supported by the discussion developed by Lele (1989) upon the vorticity dynamics of the supersonic mixing layer in the phase of transition to turbulence. The density ratio and the convective Mach number are shown to have separate effects on the spreading rate. The convective Mach number is seen to trigger the growth rate of the rollups in their moving frame while the density ratio changes their convection speed. The latter effect is finally attributed to a significative contribution of the baroclinic torque to the vorticity budget, in agreement with the incompressible analysis by Soteriou & Ghoniem (1995). The baroclinic torque is seen to yield an asymmetric vorticity field and the standard elliptic eddy is turned into a coma-shaped layer standing on the light side of the rotation center. The implications of such a redistribution of vorticity in inertia dominated low-speed flows stands as the focus of the present paper.

The present contribution thus deals with the baroclinic effects beyond the Boussinesq approximation but uncorrelated to compressibility. The baroclinic torque results from the inertial component of the pressure gradient only and the vorticity is seen to evolve in a quasi-solenoidal velocity field. This purely inertial influence of density variations is likely to occur in high Reynolds number and high Froude number mixing of fluids of different densities or in thermal mixing. Such variable-density shear-layers were previously considered by Davey & Roshko (1972) who concluded that the situation where the lighter fluid

is the faster leads to an increase in the amplification rate of instability oscillations. More recently a step further was achieved in the numerical analysis of Soteriou & Ghoniem (1995) on spatially evolving two-dimensional shear layers. They confirmed that an asymmetric entrainment resulting from the baroclinic torque is responsible for the shifting of the center of the main structures into the lighter fluid, a different convection velocity and, as stated before, a modified spreading rate. The three-dimensional study of Knio & Ghoniem (1991) set the frame for the stability analysis of the baroclinically-altered roller. However, this issue remains unanswered and it stands as one crucial target the present research.

The relevancy of such a question also emerges when considering the specific features of the cousin prototype flow, the variable-density jet. From the early work of Corrsin & Uberoi (1949) to the review by List (1982) and the late papers by Richards & Pitts (1993) and Panchapakesan & Lumley (1993), the sensitivity of the mean fields and statistical moments of fully turbulent jets to the density ratio has been extensively documented. The Reynolds shear-stress budget is demonstrated to be complemented with mean-density gradient terms that enhance the diffusion of light jets ending in higher spreading and mixing rates. Correlations with density fluctuations, i.e. turbulent mass fluxes, may be also invoqued, together with mean inertia effects, to analyse the behaviour of turbulent variable-density jets, see Chassaing, Harran & Joly (1994).

Besides, the experiments of Crow & Champagne (1971) have asserted the idea that even at high Reynolds numbers the jet dynamics and downstream evolution depends strongly on the development of deterministic vortical structures associated with amplified instability modes. The linear stability analysis reviewed by Michalke (1984), were very successful in the prediction of the preferred modes of the jet and stressed its dependancy on the radius to momentum-thickness ratio R/θ. The particular instability of low-density jets was also noticed at that time and analysed later by Monkewitz & Sohn (1988) to be an absolute instability occuring at a local density ratio below of 0.72 in the axisymmetric case. These studies were followed by both theoretical and experimental efforts that converged toward a quite unified picture of the "exotic" character of the low-density jet.

From the experiments reported by Monkewitz et al. (1990) and the similar ones by Kyle & Sreenivasan (1993), it is found that low-density jets, below the critical density ratio, exhibit both a powerful self-excited column mode and typical lateral ejections of light fluid at right angle of the jet axis. Both features are spectacularly recovered in the helium round jet by Hermouche (1996) and in the plane jets by Raynal et al. (1996). The latter underlined the influence of the distance between the velocity and density profiles inflection points.

In the previously quoted linear stability analysis, the column mode is merely acknowledged as a result of the deductive formalism of the stability analysis. It seems, though, that inertia effects embeded in the linearised description of the flow, are not well identified and that we are still lacking a cause-to-effect explanation that may extend in the non-linear regime. The numerical experiments by Grinstein, Oran & Boris (1991) are a noticeable attempt in such a direction.

This may well be crucial to design efficient control strategies to switch on the absolute mode on homogeneous jets, see Chapin, Malandra & Chassaing (1999).

As for the onset of side-jets, it is out of the scope of the linearised approaches and is often described as a by-product of the low-density jet self-excitation, see Huerre & Monkewitz (1990). In the experimental investigation performed by Monkewitz & Pfizenmaier (1991), it is concluded that pairs of counter-rotative streamwise vortices, analogous to those encountered in the three-dimensional mixing-layer, are triggering radial ejections roughly periodically spaced in the azimuthal direction. The numerical study of temporally-evolving corrugated homogeneous jets by Brancher, Chomaz & Huerre (1994) confirm this scenario stressing the persistence of Biot-Savart induced side-jets lying in the braid region between the wavy vortex rings. In both attemps it is assumed that, with respect to the side-jet mechanism, the externally forced homogeneous jets reproduce the features of the self-excited low-density jets. The comprehensive exploration of the three-dimensional stability of round jets, performed by Brancher (1996), is also based on this assumption. The last part of the present contribution aims at gathering new elements on both the onset of the column mode and the consequence of the baroclinic torque on the spontaneous occurence of side ejections in light jets.

2 The baroclinic torques

The generation-destruction of vorticity by the baroclinic torque is not a specific feature of industrial flows. It occurs in any non-barotropic flow and is a well identified process that also affect the development of geophysical flows under the Boussinesq approximation, see Turner (1973). In this situation the baroclinic torque has been demonstrated to have a strong influence on the two-dimensional and three-dimensional stability characteristics of the shear flow. It allows secondary modes to occur in the saddle point region of two-dimensional stratified shear-layers as described by Staquet (1995). It has a strong influence on the vorticity distribution of the Kelvin-Helmoltz billows that bias the spanwise stability of the three-dimensional stratified mixing layer, e.g. Klaassen & Peltier (1991), Cortesi, Yadigaroglu & Banerjee (1998) and the experimental investigation by Schowalter, Van Atta & Lasheras (1994).

While inertia dominated flows exhibit a significative internal acceleration due to the flow itself, these buoyancy dominated flows are immersed in the external gravity field, constant in direction and intensity, that combines with slight density gradients. Such externally accelerated variable-density flows are also encountered in internal combustion engines. Borée (2000) and Bury (2000) have discussed the relative competition between the time scales of the unsteadiness and the baroclinic torque in a light jet issuing in a highly pulsed coflow. Whereas unsteadiness dominates the close-to-outlet development of the jet, a transition to a baroclinically piloted behaviour occurs downstream.

Thus it turns out that the nature of the baroclinic torque depends on the nature of the acceleration field, hence the use of the plural in the title. This

section aims at clarifying the different situations where a significant baroclinic torque has to be accounted for.

It is argued here that a relevant view of the changes in flows carrying inhomogeneous density fields may be sought from the analysis of the vorticity dynamics. The compressibility and inertia effects are to be considered from the general form[1] of the vorticity transport equation :

$$\frac{\mathrm{d}\boldsymbol{\omega}}{\mathrm{d}t} = (\boldsymbol{\omega}\cdot\boldsymbol{\nabla})\mathbf{u} - \frac{1}{\rho^2}\boldsymbol{\nabla}P\times\boldsymbol{\nabla}\rho - d\,\boldsymbol{\omega} + \nu\Delta\boldsymbol{\omega} \tag{1}$$

where we find the vortex-streching mechanism first, followed by the baroclinic torque, the dilatation term, with $d = \boldsymbol{\nabla}\cdot\mathbf{u}$, and the diffusive one. This equation results from the curl of the momentum equation within the Navier-Stokes model :

$$\frac{\mathrm{d}\rho}{\mathrm{d}t} = -\rho\, d \tag{2}$$

$$\frac{\mathrm{d}\mathbf{u}}{\mathrm{d}t} = \mathbf{g} - \dot{\mathbf{u}}_r - \frac{1}{\rho}\boldsymbol{\nabla}p + \nu\Delta\mathbf{u} + \frac{\nu}{3}\boldsymbol{\nabla}d \tag{3}$$

Here, the velocity field is expressed in a possibly accelerated reference frame, which velocity is quoted $\mathbf{u}_r$. The gravity field is $\mathbf{g}$. In the limit of an infinite Reynolds number or in the inviscid situation, the pressure gradient is seen to results from the following generalized acceleration field $\mathbf{a}^*$:

$$\mathbf{a}^* = \frac{\mathrm{d}\mathbf{u}}{\mathrm{d}t} - \mathbf{g} + \dot{\mathbf{u}}_r \tag{4}$$

such that the inviscid baroclinic torque $\mathbf{b}$ may be recast in the form :

$$\mathbf{b} = \mathbf{a}^*\times\frac{1}{\rho}\boldsymbol{\nabla}\rho \tag{5}$$

The enstrophy $z = \frac{1}{2}\omega^2$ exhibits then a corresponding source/sink term that may compete with the vortex stretching, $\mathbf{s} = (\boldsymbol{\omega}\cdot\boldsymbol{\nabla})\mathbf{u}$, and dilatational enstrophy productions :

$$\frac{\mathrm{d}z}{\mathrm{d}t} = \mathbf{s}\cdot\boldsymbol{\omega} + \mathbf{b}\cdot\boldsymbol{\omega} - 2d\,z + \nu\Delta z \tag{6}$$

That comprehensive view of the different origins of the baroclinic torque may be illustrated in situations where only one of its components is active. In the pioneering work of Thorpe (1968) or in the recent numerical simulation by Andreassen et al. (1998) the gravitationnal baroclinic torque is seen to be the dominant vorticity source. Flows that this paper consider are inertia-dominated and the acceleration field results from unsteadiness only.

[1] The extra terms, coming from the viscosity dependence to the fluid composition or temperature, are discarded. For the full version see "Variable density Turbulence" by P. Chassaing in the present monography.

3 The two-dimensional mixing layer

As sketched on figure 1, the mixing layer is a downstream developing flow where a fast stream merges with a parallel and slower one. Here the density gradient and the velocity gradient are pointing upward in a so-called co-gradient mixing-layer. When the density and the streamwise-velocity gradients are in opposite directions, the situation is said to be counter-gradient. The spatially evolving flow is often associated with its time-evolving equivalent which, though suffering from different symmetry proprieties, e.g. Corcos & Sherman (1984), is a convenient model for both theoretical and numerical studies. The temporal model aims at following the time development of a streamwise portion of the flow in a frame moving downstream at the convection velocity u_c. The time may be converted back to the streamwise distance to the splitter plate by $x = u_c(t - t_0)$. The approximation is also made that, provided the length of the temporal frame is a multiple of a streamwise periodic pattern, the flow is assumed to be streamwise periodic.

The shear layer is highly unstable and develops well organized spanwise flow patterns as those observed by Brown & Roshko (1974) at high Reynolds numbers. The growth rate and the streamwise wavelength of this Kelvin-Helmholtz instability is only weakly affected by the density ratio between the two-streams, see Landau & Lifchitz (1989) P. 154, Maslowe & Kelly (1971) and Soteriou & Ghoniem (1995). Meanwhile, the flow spreading rate, the entrainment rate and the convective velocity of the eddies is known to be affected by the density ratio as reviewed by Dimotakis (1986).

The two-dimensional development of this flow is considered first with the purpose of extracting the specific features due to the baroclinic torque as seen from the vorticity and strain fields of a temporally evolving model. The occurence of a two-dimensional baroclinic secondary instability mode is then discussed before a short description of spatially developing mixing-layers.

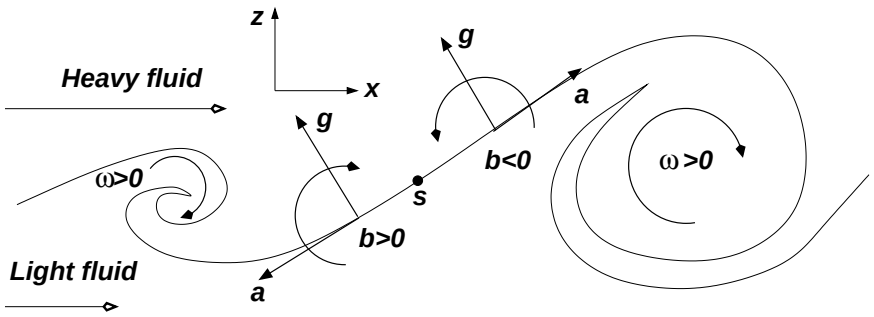

Figure 1: The sketch of the co-gradient mixing-layer between a fast heavy stream and a slow lighter one. The density gradient is $\mathbf{g} = \boldsymbol{\nabla}\rho$. Source and sink contributions of the baroclinic torque to the vorticity field are outlined.

3.1 The two-dimensional roll-up

The temporal evolution of a streamwise wavelength λ_x of the Kelvin-Helmoltz instability is considered. The streamwise velocity is $-U + u_c$ in the lower freestream and $+U + u_c$ in the upper one. The initial vorticity thickness of the error function velocity profile is quoted δ_ω^0 and is choosen to fit the most unstable mode by setting $\lambda_x = 7.3\ \delta_\omega^0$. The flow is perturbed using the eigenfunctions for $\mathbf{u}$ and ρ given by the linear stability analysis of the passive scalar situation. This shall ensure the relevancy of the comparisons between passive and active scalar situations. The phase speed of the perturbation, u_c, which is non zero in the variable density case, is superimposed on the perturbed profile in order to keep the main structure centered in the domain.

Within the temporal approximation, it is demonstrated that no differences are expected between the co-gradient and the counter-gradient configurations. The galilean transformation $(x, z) \rightarrow (x* = -x, z* = -z)$ turns one situation into the other such that replacing the density ratio $S_\rho = \rho_{\text{upper}}/\rho_{\text{lower}}$ by $1/S_\rho$ has no effect on the flow development. In the followings, the upper freestream is then arbitrarily choosen to be the heavier. The Reynolds number is defined by $\mathcal{R}_e = U\delta_\omega^0/\nu$ and the Prandtl-Schmidt number is set to unity. Normalization is performed using the scales U, δ_ω^0 and $\tau = \delta_\omega^0/U$.

In the flow configuration of figure 1, and due to the mean streamwise velocity field, upward shifted fluid lumps are experiencing a downstream acceleration while downward shifted particles are decelerated. In the temporal frame, moving at the eddy convection speed, both fluid elements are advected appart from the stationary saddle point, marked **s** on the figure. This acceleration field combined with a upward density gradient gives rise to opposite sign contributions of the baroclinic torque to the vorticity field.

Such a source-sink association led Soteriou & Ghoniem (1995) to consider the added baroclinic vorticity as a superimposed counter-rotative dipole. This dipole interpretation is very successful in explaining the asymmetric entrainment rate and the density effect on the convection speed, both expected from experimental evidence. The density field in figure 5(b) illustrates the preferencial entrainment of light fluid into the core. The shifting of the center of the eddy towards the light stream also results from entrainment asymmetry and continuity, see Soteriou & Ghoniem (1995).

This source-sink system yields first a strong asymmetry of the vorticity field, as illustrated on figure 2 and later induces a strong concentration of the circulation on thinning vorticity sheets of opposite signs. The vorticity is redistributed in favour of the vorticity braid-end pointing toward the light side (left-side of figure 3), the other end being vorticity depleted in a first stage and then fed with a vorticity source of sign opposite to the one of the initial layer. These two opposite-sign vorticity sheets wrap around an asymmetric primary structure core located at the center of the streamlines pattern, see figure 5(d). Due to i/ the alternate sign of the acceleration field along the vorticity sheets and ii/ the folding of the density field changing the direction of the density-gradient, the baroclinic torque exhibits consecutive regions of positive and negative contri-

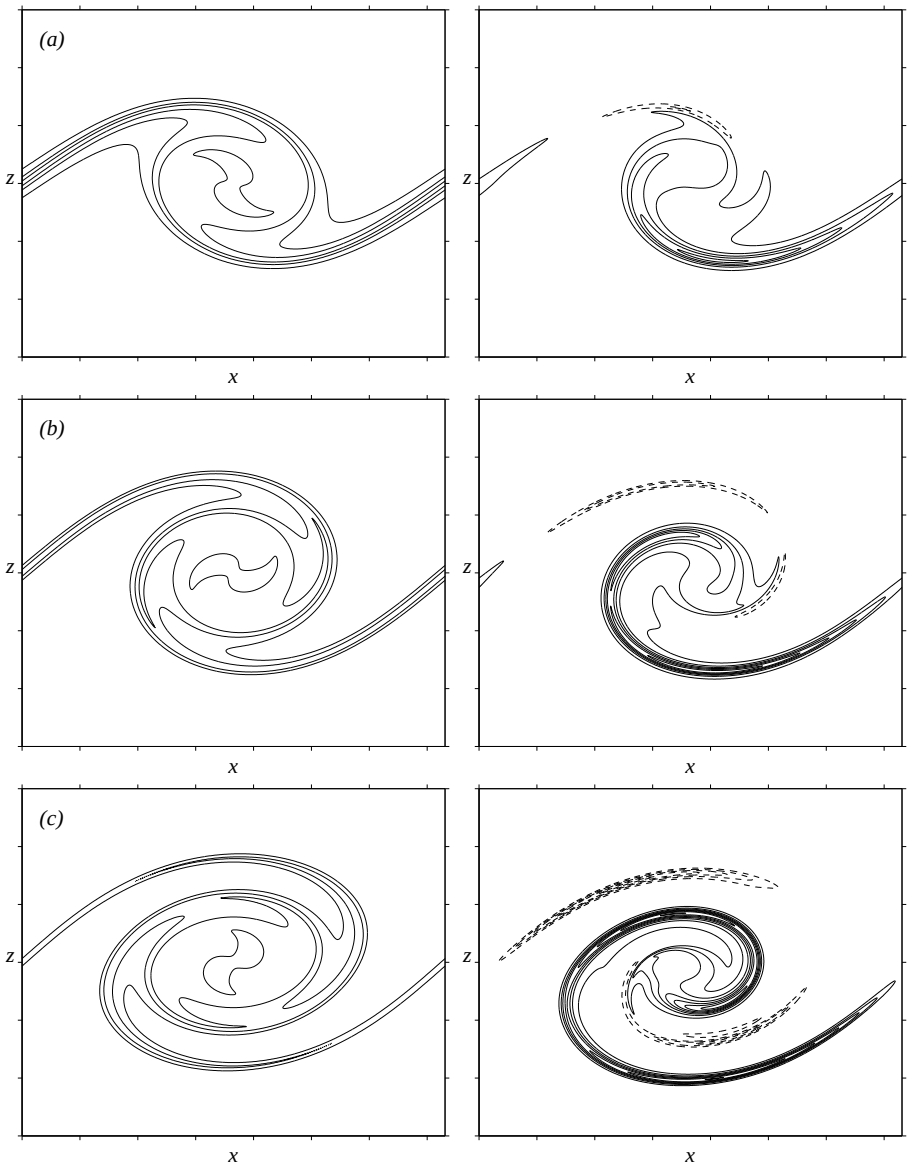

Figure 2: Vorticity ω_y contours of the two-dimensional variable density mixing-layer at $\mathcal{R}_e = 3000$. Left column : passive-scalar case, right column : variable-density situation with density ratio of $S_\rho = 3$. The time normalized by τ, is (a) $t = 8$, (b) $t = 10$, (c) $t = 12$. Contour increment is $1/2\tau$ for the passive-scalar case and twice that value for the variable-density case. The negative contours are drawn with dashed lines; tic marks along x and z coordinates are every δ_ω^0.

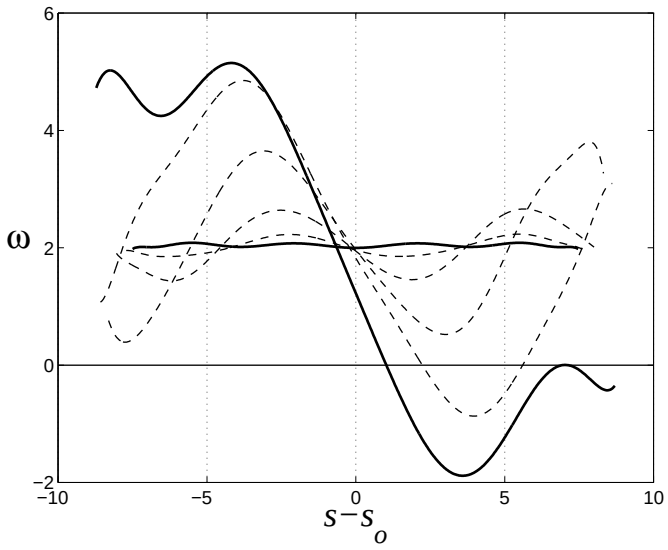

Figure 3: Normalized vorticity $\omega \times \tau$ along the central material line (where $\rho = (\rho_{\text{upper}} + \rho_{\text{lower}})/2$) of the variable density mixing layer with $\mathcal{R}_e = 1500$ and density ratio $S_\rho = 3$. The solid curves are the initial vorticity level and the one at t=10. Dashed lines are every $\Delta t = 2$ and the dot-dashed line marks the zero threshold. The abscissa is given along the normaliwed curvilinear coordinate s/δ^0_ω associated to the material line, s_o being the origin at the saddle point.

butions to the local vorticity. Figure 5(c) shows how the spatial distribution of the baroclinic torque has evolved from the simple counter-rotative dipole proposed by Soteriou & Ghoniem (1995) toward an intricate multipole after the saturation time.

Though the growth of the primary mode energy is only weakly affected by the baroclinic torque, see figure 4(b), significative amounts of negative and positive circulations are generated at both ends of the braid and within the core. These contributions have to cancel in order to fullfil the invariance of the global circulation over the period : $\Gamma_0 = 2U\lambda_x$. Figure 4(a) illustrates the departure of the positive circulation Γ^+ from that reference level. By the saturation time t_s the positive circulation has grown up to three times the initial value. A corresponding negative circulation has been generated meanwhile at the other end of the braid lying on the heavy-side of the main structure.

In contrast with the passive scalar case, where a smooth elliptic core structure is receiving advected vorticity from the strained braids (left column of figure 2), the filamentary nature of the vorticity field is more pronounced and yields a wider spectrum of energetic wavenumbers. The trend to develop this filamentary structure, since limited by viscous diffusion, intensifies with increasing Reynolds number (compare figure 5(a) and 2 bottom-right). The departure of this vortical structure from the often invoqued prototype Stuart vor-

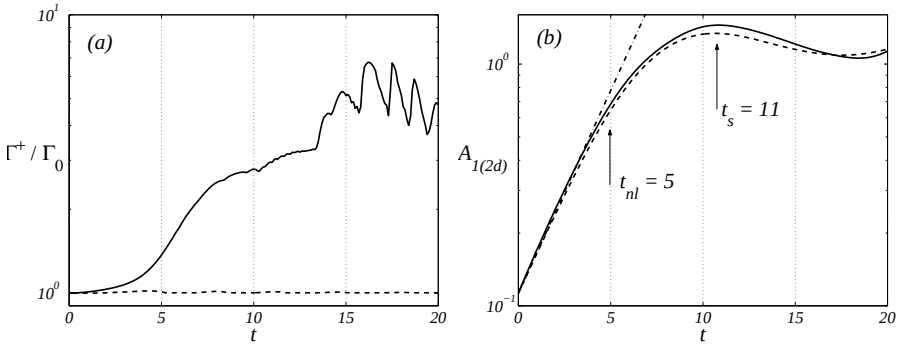

Figure 4: (a) The increase of the circulation Γ^+ associated with baroclinically enhanced positive regions of vorticity, normalized by the initial circulation Γ_0. (b) : the kinetic energy of the primary mode $A_1(2d)$, associated to the streamwise wavenumber $k_x = 2\pi/\lambda_x$. Before $t_{nl} \approx 5$ the linear analysis (dot-dashed line) predicts an exponential growth of the energy. Then the shear-layer enters a non-linear stage leading to the saturation of the K-H mode at $t_s \approx 11$. The dashed lines give the passive scalar references.

tex is striking. The streamline pattern has the same global features, see figure 5(d), excepted for the symmetries of the Stuart vortex. As noted first by Knio & Ghoniem (1992), no such steady approximation of the variable density roller is suited for the three-dimensional stability analysis of the variable-density mixing layer, a point discussed in section 4.

3.2 The variable-density shear and strain fields

As far as the mixing proprieties or the process of three-dimensionalization of this flow are concerned, a description of the 2D strain field is needed. Given the strain tensor $\mathcal{D} = (\boldsymbol{\nabla}\mathbf{u} + \boldsymbol{\nabla}\mathbf{u}^t)/2$ the question arises regarding the proper direction of examination of the strain. In a pure shear flow with $2\lambda = \mathrm{d}u/\mathrm{d}y$, 7.(a), the eigen vector of the strain tensor is tilted at $\pi/4$ of the vorticity sheet, whereas in the pure strain flow, 7.(b), the maximum stretch is obviously aligned with the streamwise direction.

$$(a) \quad \mathcal{D} = \begin{pmatrix} 0 & \lambda \\ \lambda & 0 \end{pmatrix} \quad , \quad (b) \quad \mathcal{D} = \begin{pmatrix} \gamma & 0 \\ 0 & -\gamma \end{pmatrix} \tag{7}$$

In the general case, the strain tensor has to be projected in the direction of interest to give the stretching rate in that direction. Klaassen & Peltier (1991) used simplified expressions of the shearing and stretching deformation that are valid for an horizontal line only. We choose the less ambiguous projection onto the material line, everywhere normal to the density gradient $\mathbf{g} = \boldsymbol{\nabla}\rho$.

Within the local frame of reference (t, n) of figure 6, designed for the braid region analysis by Corcos & Sherman (1976), the definition of the shear rate λ

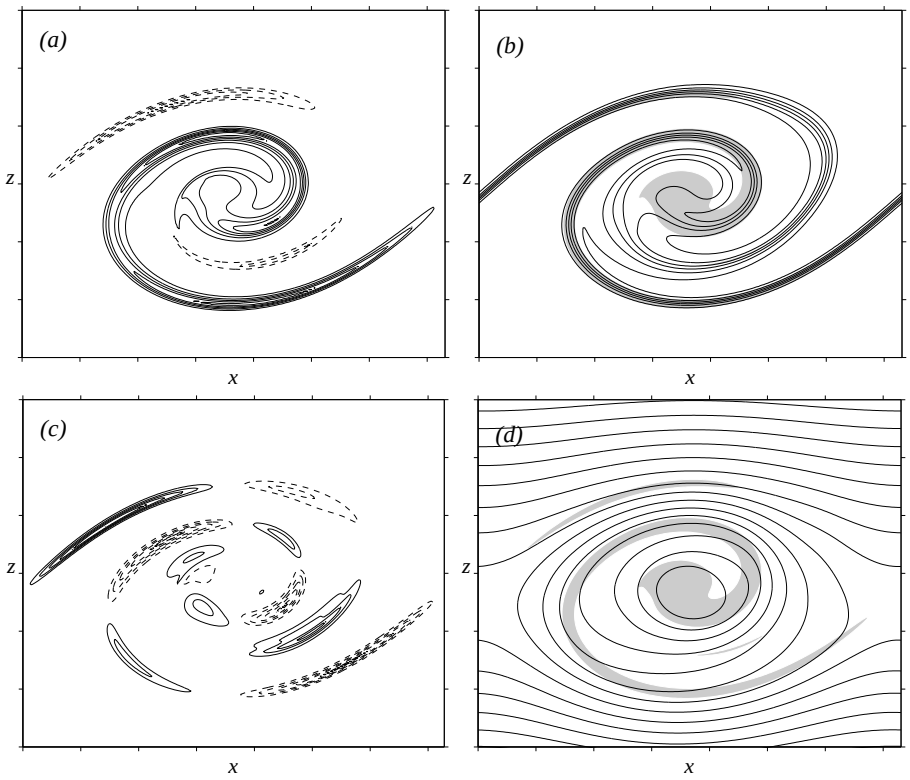

Figure 5: Description of the flow fields of the two-dimensional variable density mixing-layer at $\mathcal{R}_e = 1500$ at $t = 12$. (a) vorticity contours (increment U/δ^0_ω), (b) density contours (increment $\Delta_\rho/6$), (c) baroclinic torque (increment $0.5\delta^{0\,2}_\omega$), (d) streamlines. The negative contours are drawn with dashed lines; in figures (b) and (d), the shaded region corresponds to absolute vorticity levels above $2U/\delta^0_\omega$; tic marks along x and z coordinates are every δ^0_ω.

and strain rate γ of the material line is precisely :

$$\lambda = \frac{\partial u_t}{\partial n} \quad , \quad \gamma = \frac{\partial u_t}{\partial t} \tag{8}$$

They can also be readily given by the following tensorial analysis :

$$\lambda = \mathbf{n} \cdot \boldsymbol{\nabla}\mathbf{u} \cdot \mathbf{t} \quad , \quad \gamma = \mathbf{t} \cdot \boldsymbol{\nabla}\mathbf{u} \cdot \mathbf{t} \equiv \mathcal{D} : \mathbf{tt} \tag{9}$$

where $\mathbf{t}$ and $\mathbf{n}$ are then the unitary vectors of the local reference frame (t, n).

Figure 7 shows the evolution of the strain rate at the saddle point γ_s. It is weakly affected by the redistribution of vorticity in the main structure. According to Corcos & Sherman (1984), the strain rate at the saddle point depends on the circulation accumulated within the main structure core and plateaus after

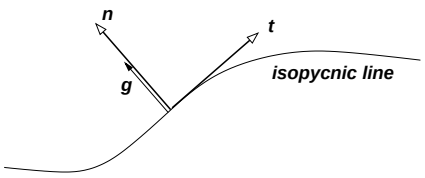

Figure 6: The local frame of reference (t, n) for the analysis of the strain rate.

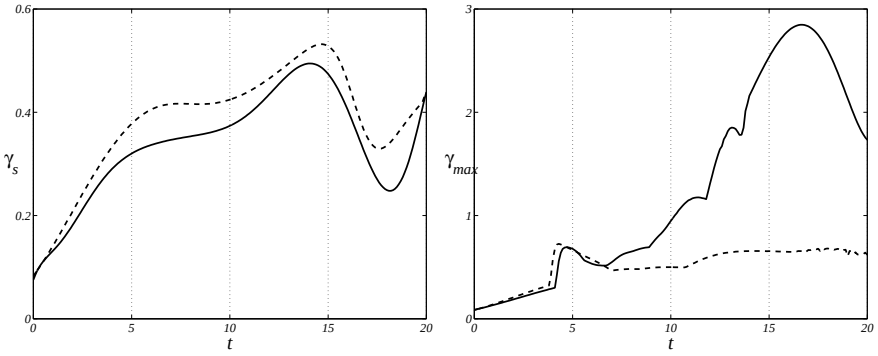

Figure 7: Left : the evolution of the strain rate γ_s normal to the density gradient at the saddle point between the main 2D structures. Right : evolution of the overall maximum of the strain rate $\gamma_{\max}$. Solid line : variable density mixing-layer at $S_\rho = 3$; dashed line : passive scalar mixing-layer.

the saturation of the primary mode instability, i.e. after t_s. In the variable-density situation the circulation is still globally invariant in the main structure, with cancelation of baroclinic source and sink terms, and the strain rate at the saddle point is thus expected to be independant of density effects.

The invariance of the circulation of the main structure does not extend to local amounts of circulation and a more detailed investigation of the stretching field is needed. On figure 7 the maximum value of the strain rate over the all field is shown to be drastically enhanced due to the new vorticity distribution. By the end of the primary mode saturation, levels of strain twice as much as their passive scalar equivalent can be found in the strain field. After $t_s \approx 11$ this level even peaks toward normalized strain rates of 3 which is four times as much as in the passive scalar situation.

The question of the location of these high strain rates is answered on figure 8 where the symmetric strain field of the passive scalar rollup at $t = 10$ and the baroclinically modified one are compared.

On figure 8(a) the shear of the passive scalar rollup is seen to be concentrated, with vorticity, in the core region. The higher strain rates (above $3/8\tau$) are found

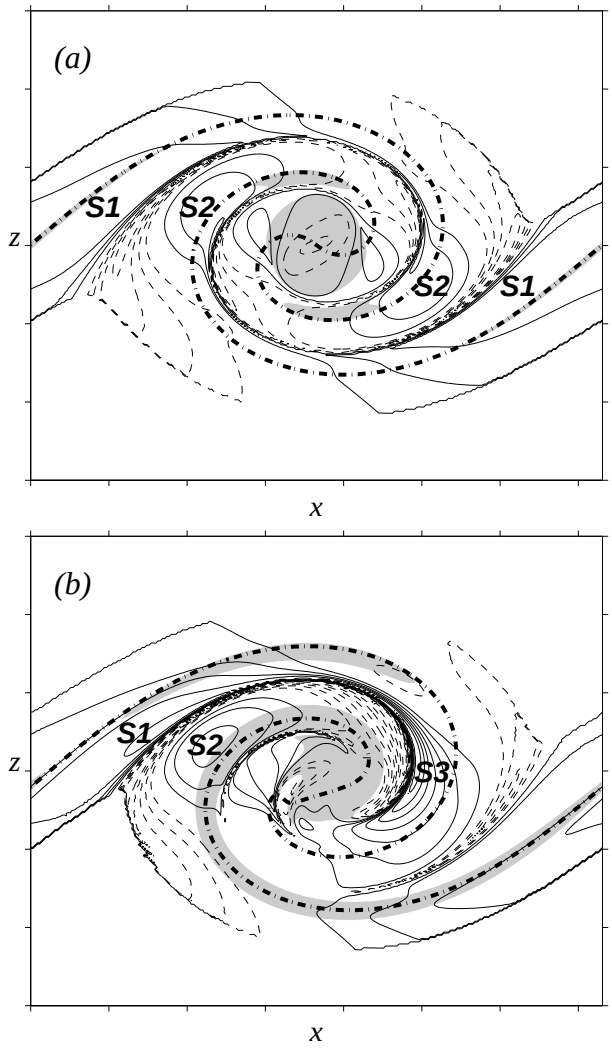

Figure 8: Contours at $t = 10$ of the strain rate γ (increment is $1/8\tau$, solid lines for positively stretched region, dashed line for negative strain rate or compression), and the shaded region correponds to shear rates $|\lambda|$ above $1/\tau$, the thick dot-dashed line is the central material line : (a) passive scalar case, (b) variable density mixing layer with $S_\rho = 3$.

on the braid, in region $\boldsymbol{S1}$, centered around the saddle point and spreading on both sides of the central material line. Secondary regions of high stain (locally reaching $3/8\tau$), marked $\boldsymbol{S2}$, are located near the center of the structure core and concern the light or heavy fluid lumps entrained into the eddy.

The figure 8(b) indicates the clear asymmetric develoment of the shear and strain fields. Due to the intense baroclinic torque, the left-end of the braid is submitted to a shear rate four times as high as in the passive scalar rollup. Besides, three regions of high strain rates are clearly identified. The regions $\boldsymbol{S1}$ and $\boldsymbol{S2}$ of figure 8(a) are recovered, but region $\boldsymbol{S1}$ is shifted downward into the lighter fluid region where the strain rate reaches values above $5/8\tau$. The region marked $\boldsymbol{S3}$ holds the absolute maximum of the strain rate at $t = 10$ above $7/8\tau$ in agreement with figure 7.

The baroclinic torque is seen to enhance the shear rates and reorganise the strain field. The lighter part of the mixing layer is then submitted to much higher strain at the center and at the ends of the braid. Such a detailed description gives the first elements that may lead to a better understanding of the development of three-dimensional streamwise structures through the vortex stretching mechanism.

3.3 The two-dimensional baroclinic secondary instability

At infinite Reynolds numbers Reinaud, Joly & Chassaing (2000) showed that the vorticity-enhanced side of the braid is likely to break-up into two-dimensional secondary rollups as illustrated on figure 9. Using an inviscid vortex element method, Reinaud (2000) identified the mechanism of this two-dimensional secondary instability. The secondary structures of Kelvin-Helmholtz type are growing spatio-temporally from amplified disturbances issuing from the saddle point region. On figure 10 the crosswise oscillations of the central isopycnic line (s, z) are given with reference to the position of a regularised curve (s, z_r) obtained by a sixth order polynomial regression of (s, z). The oscillations are more amplified on the left-end of the braid. The conditions of this amplification are discussed with the aid of a simplified model for the strained variable-density braid.

The frame of the stability analysis of a strained vorticity strip is given by Dritschel et al. (1991). The strain is seen to have a two-fold stabilizing effect. It compresses the flow in the crosswise direction and stretches the wavelength of upcoming perturbations far beyond the most amplified wavelength to strip-thickness ratio. In the case of a uniformly strained constant vorticity strip, a strain to vorticity ratio of 0.25 is sufficient to prevent any disturbance amplification. Below that threshold the growth is still very slow at 0.065 but time intervals of positive amplification rate are observed that favours the break-up of the strip into vortices. This criterion has been usefully recasted by Staquet (1995) for the stability analysis of the baroclinic layer in the stratified mixing layer under the Boussinesq approximation. It is reconsidered here and in Reinaud, Joly & Chassaing (2000) for the stability analysis of the braid region of the inertia-dominated variable-density mixing layer.

A simplified model of the variable density braid is proposed as sketched on figure 11 and it consists in a uniformly strained vorticity and density-gradient strip. The straining velocity field is $\mathbf{u}_\gamma = (\gamma x, -\gamma z)$. The initial vorticity on the strip is $\omega_0 > 0$, the uniform density is ρ_0 and the transverse positive density gradient $g_0 > 0$. Due to the strain-induced exponential growth of the

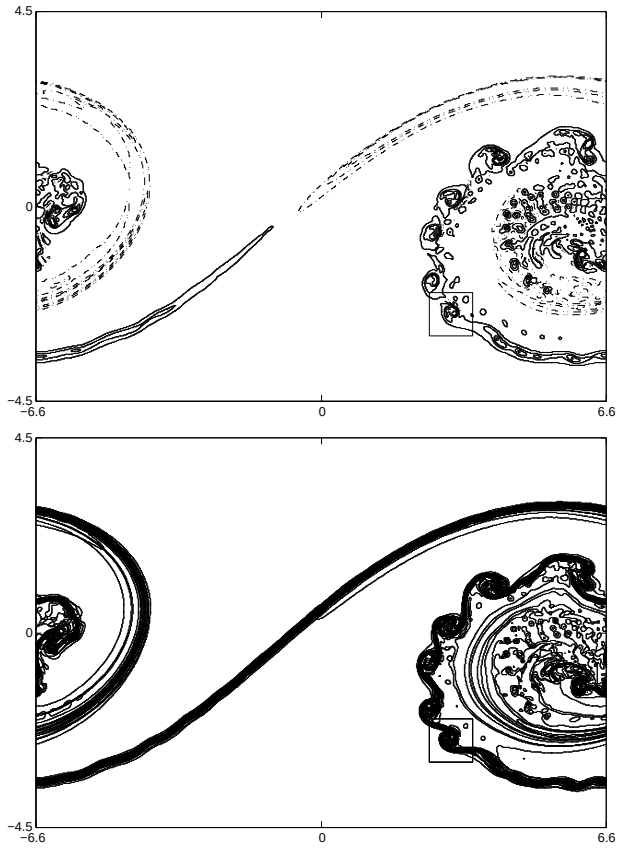

Figure 9: The secondary rollup of the baroclinically enhanced vorticity braid at $t = 12\delta_\omega^0/U$ from Reinaud (2000). (Top) Vorticity contours : solid line for positive vorticity, dahsed lines for negative ones. (Bottom) Density contours.

density gradient $g_z = g_0 \exp(\gamma t)$ and to the acceleration associated with $\mathbf{u}_\gamma$, the temporal evolution of the vorticity on the strip is given by :

$$\omega(x,t) = -\frac{\gamma g_0}{\rho_0}\, x\, \sinh(\gamma t) + \omega_0 \tag{10}$$

Note that the x-linear evolution of the vorticity is recovered along the curvilinear coordinate s on the braid of the mixing layer as illustrated on figure 3. The model predicts an exponentially growing source of positive vorticity for negative abscissa and a corresponding negative vorticity supply at far positive locations. Near the origin, a transitory decrease from the initial vorticity level is expected. The strain to vorticity ratio evolves with an inverse trend, going to zero at far ends of the vorticity strip, thus yielding perturbation-sensitive behaviours there. Moreover, given a strain to vorticity ratio threshold, the positions at which that

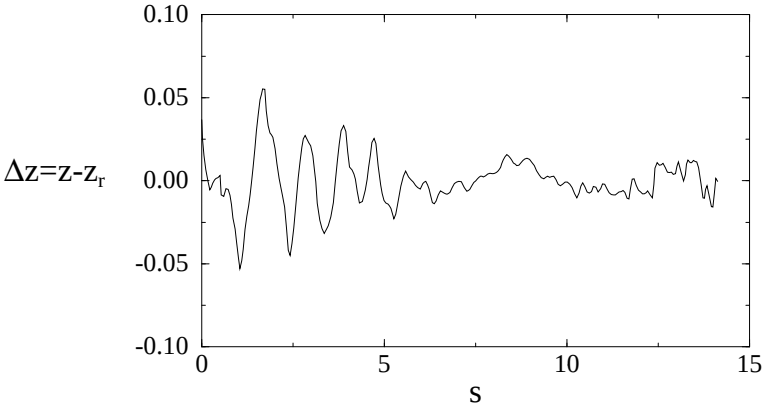

Figure 10: Crosswise oscillations of the central isopycnic line along the the curvilinear coordinate s from Reinaud (2000)

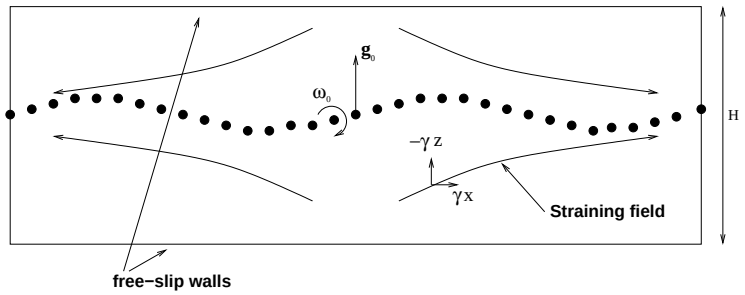

Figure 11: A simplified model of the variable-density vorticity strip submitted to a parallel uniform strain, from Reinaud (2000)

threshold is reached are getting closer to the origin with time.

This prediction is confirmed by a vortex-method simulation of a truncated version of the simplified model of figure 11. The analysis of the results is performed based on the following Helmholtz decomposition of the crosswise velocity : $v = v_\gamma + v_\omega$. The potential component of the transverse velocity v_γ is due to the strain field, and v_ω is the solenoïdal component induced by the vorticity distribution. Time is normalized by $1/\omega_0$ and length scales by λ_0, the initial wavelength of the perturbation.

At $t = 2$ on the figure 12(left) the transverse velocity in section A is dominated by its stabilizing potential component v_γ, whereas in section B the dominant rotational component v_ω works at amplifying the undulations of the strip. A neutral region stands in-between where the whole transverse velocity v collapses, indicating a neutral behavior against the stability analysis. Later on, at $t = 4$ the region A becomes neutrally stable and B is clearly dominated by the

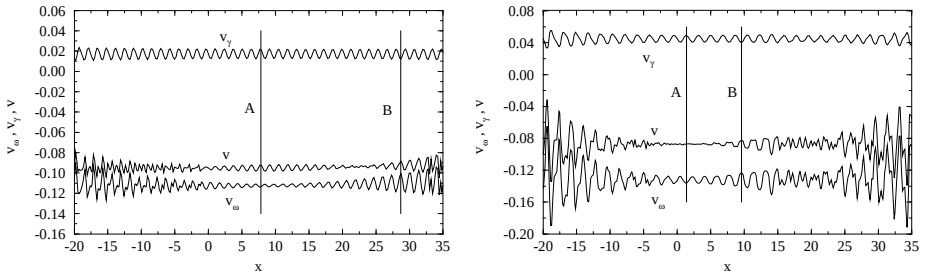

Figure 12: The distribution of the decomposed transverse velocity on the truncated vorticity/density-gradient strip at $t = 2$ (left) and $t = 4$ (right),from Reinaud (2000).

crosswise oscillation due to v_ω.

It is concluded that the baroclinic torque, favoured by the acceleration and the higher density-gradient, both produced by the strain field, significantly increases the receptivity of vorticity layers to perturbations, possibly yielding secondary rollups of the vorticity braids. This inviscid analysis has to be moderated when dealing with finite Reynolds number flows. The damping of density gradients by molecular diffusion is responsible for the smoother development of the variable density braid observed in section 3.1.

3.4 The spatially evolving variable-density mixing-layer

In figure 13 the shape of forced spatially developing mixing layer is presented from the position of vortex elements carrying the Lagrangian description of the vorticity and density-gradient. The mixing layer is bounded crosswise by two free-slip walls, separed by the channel height h, in order to suppress the rotation due to the truncation operated at the outgoing boundary conditions, see Reinaud (2000) for the assessment of the implemented boundary conditions. The phase of the given snapshots, relative to the harmonic splitter plate oscillations, is the same, such that the sensitivity of the convection velocity to the density ratio is effectively restituted. As expected the counter-gradient case (a) exhibits a lower convection velocity than the co-gradient case (c), the passive scalar mixing layer (b) being an intermediate situation. The entrainment rate, measured from the mean density profiles is also affected according to the experimental data analysed by Dimotakis (1986) and the previous Lagrangian simulations by Soteriou & Ghoniem (1995).

The second influence of the density ratio is felt from the spatial development of the pairing process. As already stated by Soteriou & Ghoniem (1995) the counter-gradient pairing occurs on a different mode when compared to the constant density and the co-gradient pairings. In the latters, two primary structures spiral toward one another at section $x = 3h$ and share downstream their circulations to form a larger and wider structure. In the former counter-gradient case, the primary structures are getting closer with downstream distance and

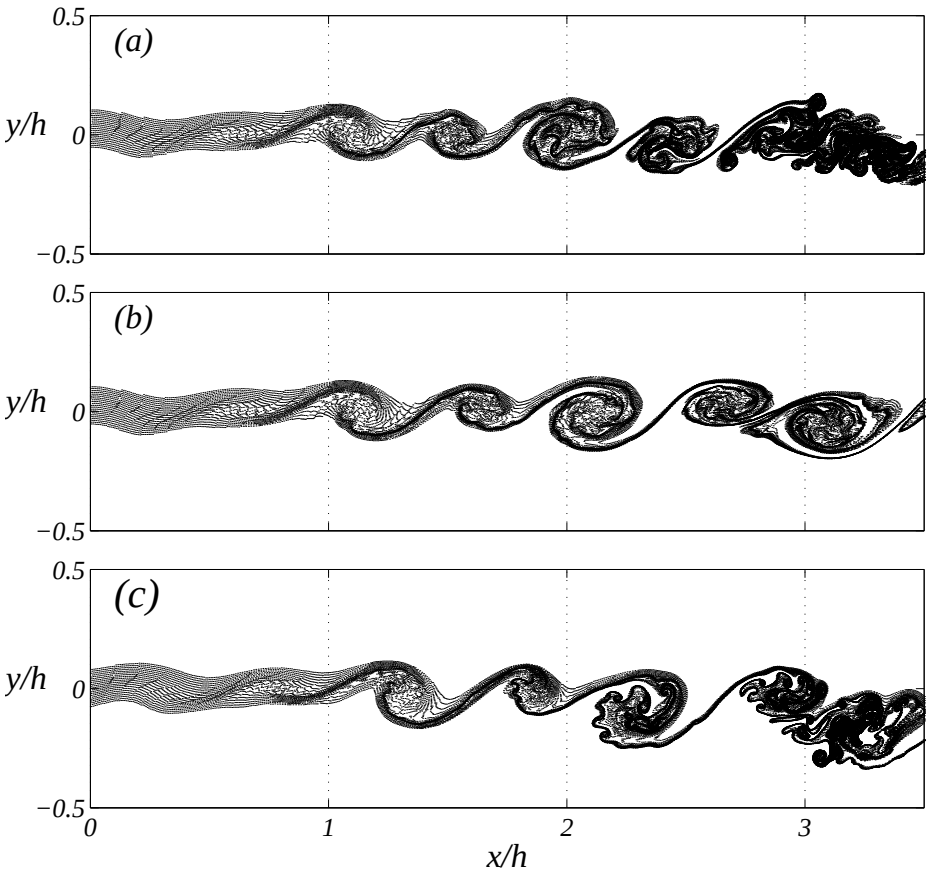

Figure 13: The spatial development of mixing layer from the position of the vortex elements : (a) counter-gradient with $S_\rho = 1/3$, (b) constant density case, (c) co-gradient with $S_\rho = 3$, from Reinaud (2000).

amalgamate into a composite new structure of a wider streamwise extent but with same crosswise thickness as the original eddies.

Here, such differences in the spatial development of the pairing process are being blured by the other obvious and original feature of these nearly-inviscid simulations, namely the quick occurence of the secondary roll-ups predicted by the temporal simulations. In both the counter-gradient and co-gradient cases, the pairing process has to occur on primary structures that have been modified by intense baroclinic vorticity sources, yielding sub-structures, less regularly organized, but similar in nature to the secondary roll-ups of the temporal simulations. Near the outlet section of the counter-gradient mixing-layer, small grained rollers can be observed even on both sides of the long structure resulting from the amalgamation of primary ones.

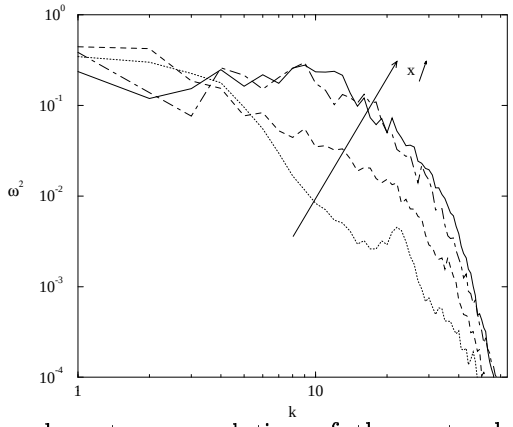

Figure 14: The downstream evolution of the enstrophy spectrums, from Reinaud (2000).

The spreading of the enstophy spectrum with the downstream distance to the splitter plate is given on figure 14 in the co-gradient case. Due to the distribution of vorticity on thinning sheets and to the secondary instability, the transition to turbulence is expected to be much quicker in variable-density mixing layers, a point favourable to an efficient mixing in reacting flows.

4 The structure of the 3D shear-layer

In three-dimensional flows the vorticity dynamics is affected by the vortex stretching mechanism that enables enstrophy to travel among vorticity components through 3D instability modes. The consequences of the baroclinic redistribution of spanwise vorticity on the development of three-dimensional modes is the focus point of this section. The interference with the pairing process and further subharmonics emergence is not yet considered.

The experimental evidence, e.g. Bernal & Roshko (1986), the stability analysis by Pierrehumbert & Widnall (1982)and Corcos & Lin (1984), and the direct simulations, e.g. Rogers & Moser (1992), all converge toward a similar route to three-dimensionality leading to streamwise vortices lying in the braid region as a result of both an instability located in the Kelvin-Helmoltz (KH) billow called translative instability (TI) and one located in the vorticity-depleted braid hereafter called shear instability (SI). Knio & Ghoniem (1992)contributed to the first analysis of these co-working mechanisms under non-symmetric vorticity conditions resulting from a weak baroclinic torque. They focussed on symmetry losses and acknowledged for uneven intensification and weakening of the streamwise vorticity.

As stated by these authors the baroclinic torque is responsible for such a different two-dimensional structure that the results on the spanwise stability of Stuart vortices or even the KH billow are irrelevant to the three-dimensional

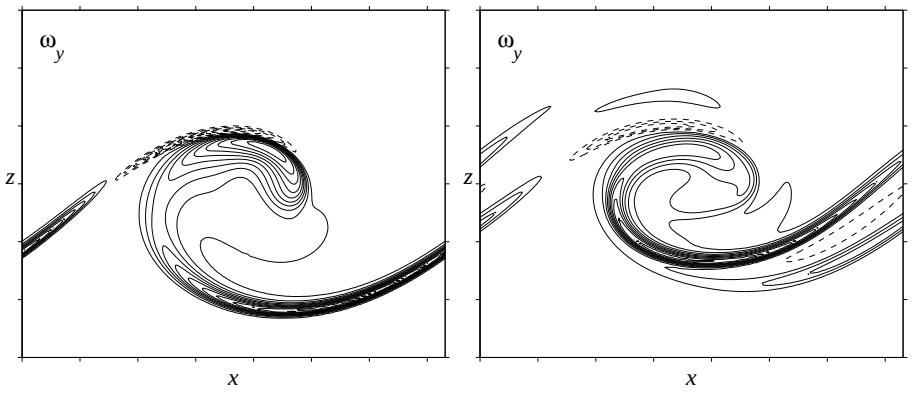

Figure 15: Contours of spanwise vorticity ω_y of the three-dimensional variable density mixing-layer at $t = 8$. Top : Base Plane cross section, bottom: Rib Plane cross section.

stability properties of the variable-density situation. Though this case demands a currently unavailable stability study, a step further has been attempted in intensifying the density variation and refining the crosswise description of the layer in order to get a full baroclinic torque effect, i.e. opposite-sign vorticity sheets as in Reinaud, Joly & Chassaing (1999). The core being vorticity depleted in favour of surrounding vorticity cups, the translative instability mechanism is expected to weaken leaving vorticity cups submitted to the braid instability. This scenario is examined here.

Two simulations are analysed in this paper, one solving the passive scalar (PS) equations and the other (VD) with full variable density effects. The parameters of the PS and VD cases are reported in table 1. Throughout the paper,

Name	ρ_{up}/ρ_ℓ	$\mathcal{R}_e$	N_x	u_c	Γ_x/Γ_y^0
PS	/	500	128	0.	0.023
VD	3	500	192	0.28	0.023

Table 1: .Global parameters of the passive scalar and baroclinically modified three-dimensional simulations

time is normalized by $\tau = \delta_\omega^0/U$, vorticity by the initial maximum $2U/\delta_\omega^0$ and strain by $1/\tau$. Unless quoted, the vorticity contours increment is always U/δ_ω^0 starting from zero. The positive vorticity contours are sketched by solid lines and negative contours by dashed ones. The tic marks along the spatial coordinates are distributed every δ_ω^0.

The structure of the spanwise vorticity cross-section is derived directly from the folded distribution established in 2D. In both the rib plane and the "off-rib" one, spanwise vorticity is redistributed in thin sheets of alternate signs. The contour maps given in figure 15, taken at $t = 8$, are still simple. In the "off-rib"

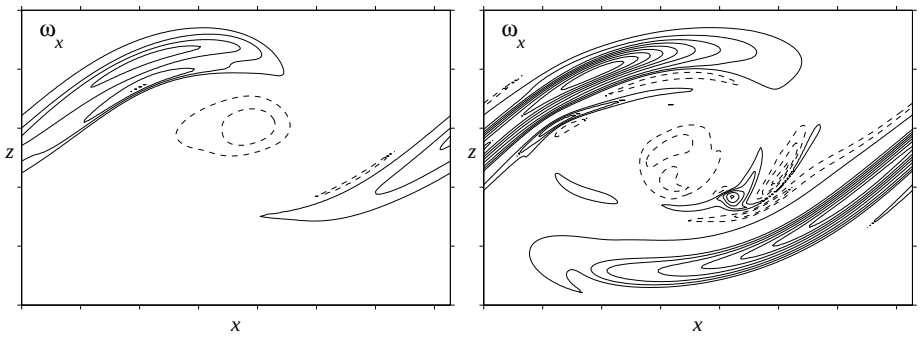

Figure 16: Contours of streamwise vorticity ω_x at $t = 8$ (left) and $t = 12$ (right). Contour increments is U/δ^0_ω, tic marks are at δ^0_ω.

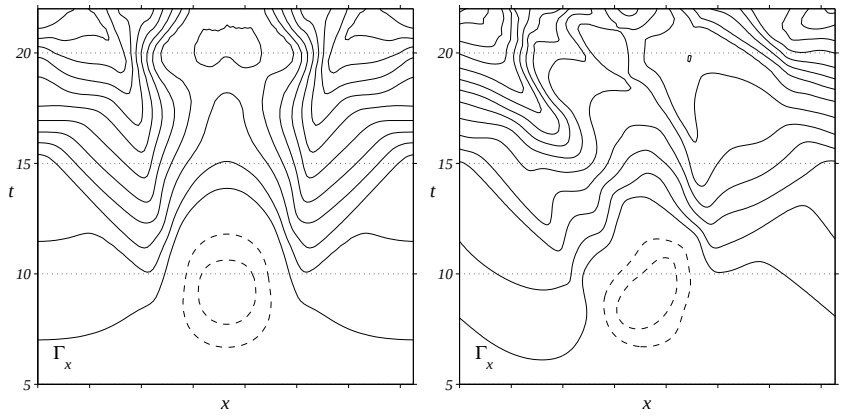

Figure 17: Time evolution of the streamwise circulation $\Gamma_x(x,t)$. Left : passive scalar, right : variable density.

base plane, cutting the center of the upper spanwise mushroom structure, two counter-rotative thin vorticity layers are brought closer to each other than in the 2D case, locally defining a jet flow of light fluid towards the heavy side. In the rib plane, the sketch is quite similar, though no more symmetric, to the one given by Rogers & Moser (1992) fig. 19(a). The analysis of subsequent spanwise vorticity maps is more difficult due to the complex structure of the core region as seen from the streamwise vorticity contours of figure 18.

Streamwise vorticity is collapsing into rib vortices as in the constant density case. At $t = 8$, figure 16 indicates that the streamwise structure is growing more rapidly on its right side lying above the main structure. This can be clearly associated with the favourable effect of the additional strain in that region, as mentioned in the 2D analysis. A weak region of negative streamwise vorticity is also noted at the center of the core and is the signature of the still

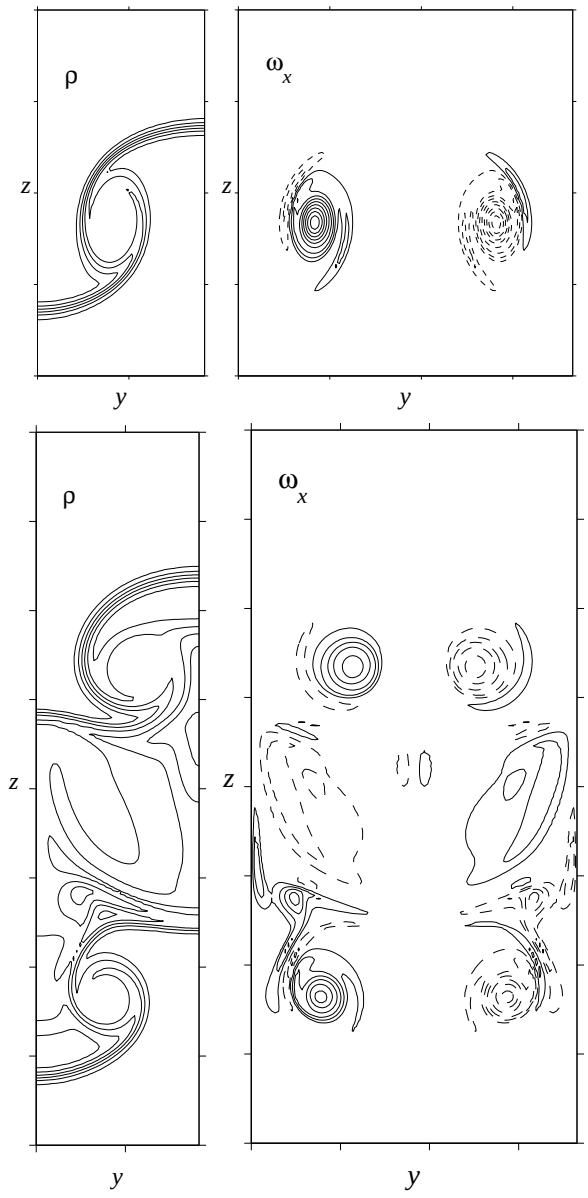

Figure 18: Contours of density and streamwise vorticity of the three-dimensional variable density mixing-layer at $t = 12$. Contour increments for the density (left) are $\Delta\rho/6$. Top : Mid-braid cross section, bottom: Core plane cross section.

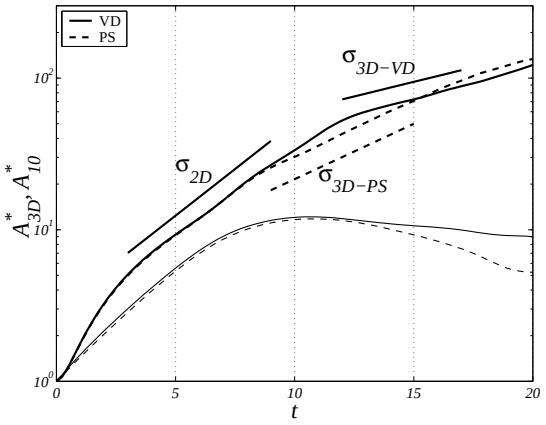

Figure 19: Time evolution of the normalized energy in all three-dimensional modes A_{3D} and in the two-dimensional one A_{10}.

active translative instability mechanism. At $t = 12$ the main contribution to the streamwise circulation comes from the dominant rib vortices, see figure 17.

The mechanism acting on spanwise vorticity in 2D, namely the baroclinic source on the light side and sink on the heavy side, is recovered in the streamwise direction. From figure 18 (right views) the rib vortices are developing with a companion counter-rotative layer on the heavy side. This association yields again a higher entrainment of light fluid into the heavy medium as seen from the density half maps.

The spatial structure of the rib vortices is seen to be affected by the modified strain field and by the streamwise baroclinic torque. The sensitivity of the amplification rate of the three-dimensional modes to these changes is discussed. Figure 19 gives the time evolution of the energy content of the pure two-dimensional mode A_{10}, corresponding to the streamwise and spanwise wavenumbers $(k_x, k_y) = (2\pi/\lambda_x, 0)$, and of the cumulated three-dimensional modes , i.e. those which satisfy $k_y \neq 0$. In this semilog plots the slopes of linear portions are equivalent to the exponential amplification rates of the small perturbations. Both the PS and VD cases undergo a two-stage evolution for A_{3D} , the first one connected with the growing 2D mode and the second one specific of the three-dimentionalization of the flow. The VD exhibits a delayed transition at $t = 12$ (9 for PS) and a lower amplification rate $\sigma_{3D-VD} = \sigma_{3D-PS}/2$. This first conclusion stands for the linear response of the layer to the presently small perturbations. The non-linear regime as well as the higher Reynolds number domains have to be further explored.

5 The structure of variable-density Jets

5.1 The two-dimensional jet

The temporal evolution of a light jet is considered with respect to a passive scalar jet, similar in all respects but the inhibition of the baroclinic torque in the vorticity equation. Both are developping the jet instability over perturbed mean velocity and mean density profiles of the hyperbolic tangent family :

$$F(z) = \frac{1}{2}[1 + \tanh\{\frac{R}{4\theta}(\frac{1}{z} - z)\}] \tag{11}$$

$$U(z) = U_\infty + U_s F(z) \qquad \text{and} \quad \rho(z) = \rho_\infty + \rho_s F(z) \tag{12}$$

where U_∞ and ρ_∞ are the velocity and the density of the surroundings. U_s and ρ_s are the jet excess velocity $U_{\text{jet}} - U_\infty$ and the density excess $\rho_{\text{jet}} - \rho_\infty$. Let the velocity ratio be $r = U_\infty / U_s$. The density ratio $s = \rho_{\text{jet}}/\rho_\infty$ is recovered from $1 + \rho_s/\rho_\infty$. Note that the velocity ratio used by Huerre & Monkewitz (1990) is $\Lambda = 1/(2r+1)$. The velocity is normalised by U_s, the spatial coordinates by the radius or half height $R = D/2$ and the time by $\tau = R/U_s$. The Reynolds number is given by $\mathcal{R}_e = U_s D/\nu$ and the Schmidt number is set to unity.

The perturbation is the most unstable mode resulting from the linear stability of the homogeneous two-dimensional jet. According to Brancher (1996), for a radius to momentum thickness ratio of $R/\theta = 11$ this mode is characterised by the streamwise wavelength $\lambda_x = R/0.41$ and the expected group velocity of the pertubation is $c_r = U_\infty + U_s/2$. The temporal analysis may be transformed back to the spatial development of the colowing jet by the transformation $x = c_r(t - t_0)$. The mode frequency of the spatial jet $f = c_r/\lambda_x$ building the Strouhal number $S_t = f\,D/U_{\text{jet}}$, may hence be given by $S_t = R/\lambda_x$ for the jet in quiescent surroundings for which $r = 0$. Because of the global convection by the coflowing velocity U_∞ and due to the density effect on the convection velocity c_r, a more general form for the temporal equivalent of the Strouhal number is :

$$S_t = G(r,s)\; R/\lambda_x \tag{13}$$

Since the group velocity is seen to increase with increasing density ratio, the low-density jet ($s < 1, r = 0$) exhibits then a lower convection velocity : $c_r < U_s/2$ and a larger spreading rate. As for the mixing layer simulation, the mean velocity profile is here added a negative coflowing velocity that ensures a steady domain-centered position of the main structure.

Figure 20 illustrates the comparison between the vorticity fields of the two-dimensional primary mode of a passive scalar jet, with $(r,s) = (-0.5, 1.)$, and the vorticity fields in a variable-density jet, with $(r,s) = (-0.4, 0.33)$. Due to a doubled increment between vorticity contours and the increased number of contours in the variable density jet, it is clearly seen that the vorticity field is highly contrasted in response to significative baroclinic sources and sinks. At first sight the primary structure is similar to the one encountered in the two-dimensional mixing layer and exhibits a similar streamline pattern as the one

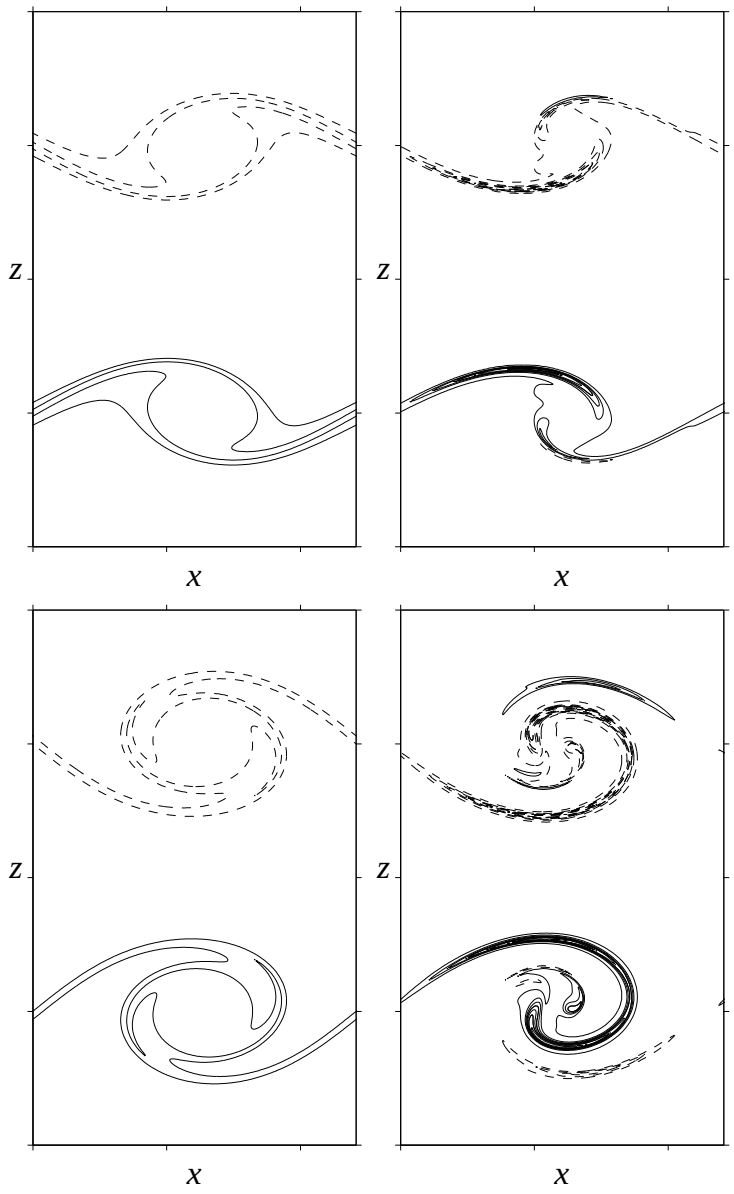

Figure 20: Vorticity ω_y contours of the two-dimensional variable density jet at $\mathcal{R}_e = 5000$. Left column : passive-scalar case, right column : variable-density situation with density ratio of $S_\rho = 3$. The time, normalized by τ, is $t = 4.5$ (top), $t = 6.8$ (bottom). Contour increment is $1/\tau$ for the passive scalar case and $2/\tau$ for the low-density jet. The negative contours of ω_y are dashed and tic marks along x and z coordinates are every jet radius.

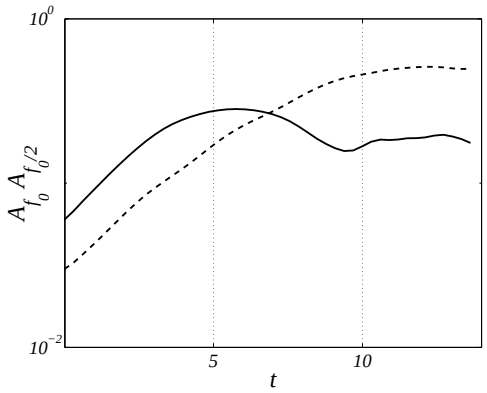

Figure 21: Modal energy of the primary mode A_{f_0} (solid line) and of the subharmonic mode $A_{f_0/2}$ (dashed line) in the case of the low-density jet with $s = 1/3$, $\mathcal{R}_e = 5000$ and $R/\theta = 11$. The primary-mode saturation time is $t_s(f_0) = 6\tau$ and the subharmonic one is $t_s(f_0/2) = 12\tau$.

given on figures 5 and 8. Any difference may be infered from the symmetry constraint on the axis, a constraint which increases with decreasing values of R/θ.

Due to the streamwise periodicity, the initial circulation over say the lower half of the jet is $\Gamma_o = U_s \lambda_x$. Since the far velocity field is uniform at $z \to -\infty$ the departure of the circulation from this initial value may be due to an evolving contribution of the streamwise velocity on the axis. It is readily given by :

$$\Gamma(t) - \Gamma_0 = \int_0^{\lambda_x} \{u_x(x, 0; t) - U_{\text{jet}}\} \, \mathrm{d}x \tag{14}$$

The present simulations result in a perfect cancellation of vorticity sources and sinks such that the integral on the right of equation 14 is zero and the circulation over the half of a temporally-evolving variable-density jet is found to be invariant. The integral in equation 14 must then vanish and the positive and negative fluctuations around the mean axial velocity cancel. However, due to the radically different distribution of vorticity in the structure, the symmetry axis does not see the same streamwise velocity. Considering the Biot-Savart law, it is expected that the contribution from the closer and baroclinically enhanced vorticity sheets are yielding a higher induced velocity at sections coincident with the streamwise position of the main structure in the low-density jet.

This conjecture is further examined on the more complete configuration where the first pairing mode is excited and developes over the primary one. The chronology of the flow development is given on figure 21. According to the standard findings, the primary modes saturates first and, with the pairing onset, the subharmonic mode energy increases untill it saturates too.

Figure 22 describes the vorticity field of the low-density jet at the saturation times of the fundamental and subharmonic modes, together with associated

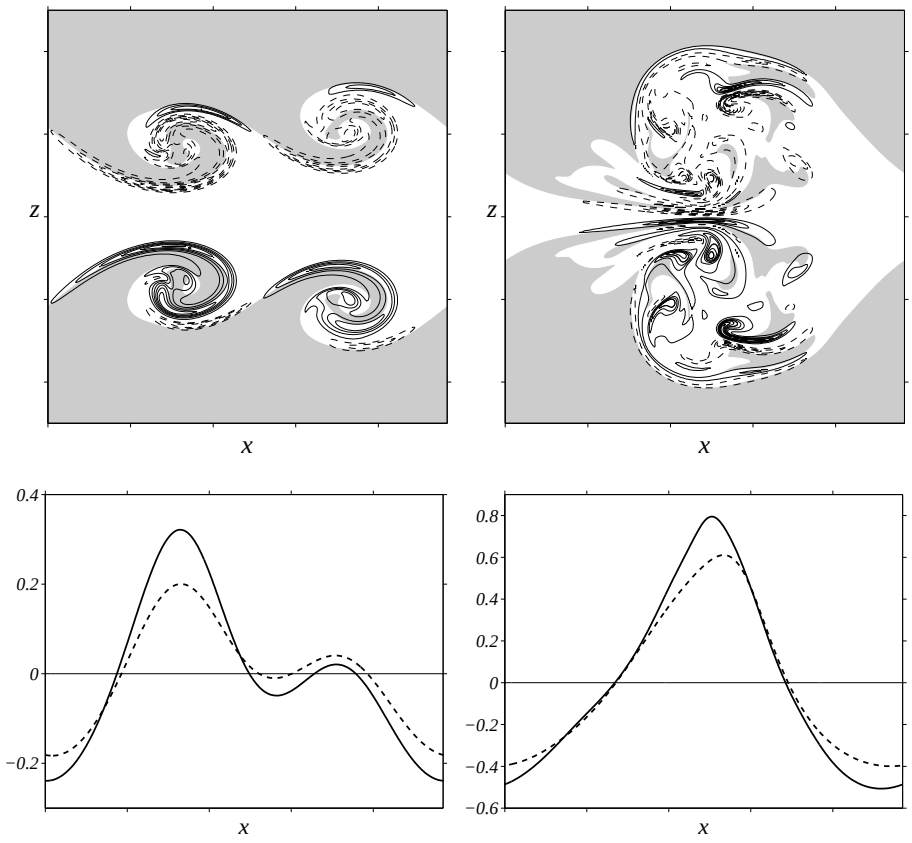

Figure 22: Vorticity contours of the two-dimensional low-density jet at $\mathcal{R}_e = 5000$ and $s = 1/3$. Left column : $t = 6$ contour increment is $1/\tau$. Right : $t = 12$ contour increment is $2/\tau$. The negative contours of ω_y are dashed and tic marks along x and z are every jet radius. The shaded area corresponds to heavy fluid of density above the mean density $\rho_{\text{jet}} + \rho_s/2$. Bottom view are the corresponding normalised on-axis streamwise velocity $(u(x,0) - U_{\text{jet}})/U_s$ compared to axis velocity profiles of the passive scalar jet (dashed lines).

axis profiles of the streamwise velocity. The baroclinic torque has redistributed vorticity, enhancing the contribution close to the axis. During the pairing event, the axis region is being pinched between intense vorticity sheets with the rapid engulfment of the upstream structure into the downstream one. This has to be related with experimental facts from the visualisation given on figure 9 by Monkewitz et al. (1990) and from the movie frames on figure 6 of the paper by Kyle & Sreenivasan (1993). Both are clearly supporting such a "pair-and-pinch" scenario of the low-density jet as it is seen also from the shaded density field in figure 22. Since the vorticity fields are not easily measured, the former paper merely concludes that the vorticity is concentrated in the streamwise direction in oscillating light jets. It can be confirmed here that due the baroclinic torque, the vorticity is much more concentrated in the crosswise direction.

The two previously cited papers also focus on the spectral and statistical content of centerline velocity fluctuations and near-field pressure fluctuations. Both are indicating higher fluctuations in low-density jets with a peak intensity located at the pairing downstream location. Here the axial velocity profile is seen to be accordingly more contrasted for the light jet then for the homogeneous jet. During the primary rollup the peak value is 50% higher and close to 30% higher during the pairing event. Besides, the velocity defect is seen to be very close to -0.5 near the head of the pairing structures, indicating a close to stationnary region in the equivalent spatial jet and a slight reversal flow in the moving temporal frame. The higher extrema centerline velocities contributes to the observed powerful fluctuation spectra. It is inferred here that this baroclinically-modified induction mechanism on the centerline of the jet is connected with the observed column mode of low-density jets. If any pressure feedback effect is to be invoqued in a compressible context, it must be noted also that the radiated noise from the baroclinically modified main structure is different from the one radiated by the smooth monopole of the homogeneous or passive scalar jet.

The profile of the streamwise velocity on the jet centerline reveals also much higher strain rates, $\gamma \approx \partial u_x/\partial x$, in the core region located before the main rollup. Such a difference may give a clue for the enhancement of streamwise vorticity in the braid region of round jets and increase thus the induced radial velocities responsible for side jets according to the proposed scheme by Brancher, Chomaz & Huerre (1994). A sounder explanation may then be proposed that links the vorticity dynamics of the fundamental axisymmetric mode with the generation of side jets. This issue is illustrated on three-dimensional simulations of temporally evolving corrugated jets.

5.2 Corrugated axisymmetric light jets

The corrugation of a nozzle has been widely considered to be an efficient device to promote mixing in industrial applications. When the corrugation is slight, it is also considered to be a relevant case for testing the onset of three-dimensionality and transition to turbulence on axisymmetric jets, see Martin & Meiburg (1991). We present here an illustration of the baroclinic torque influence on the development of a corrugated temporally evolving low-density jet. The base flow is

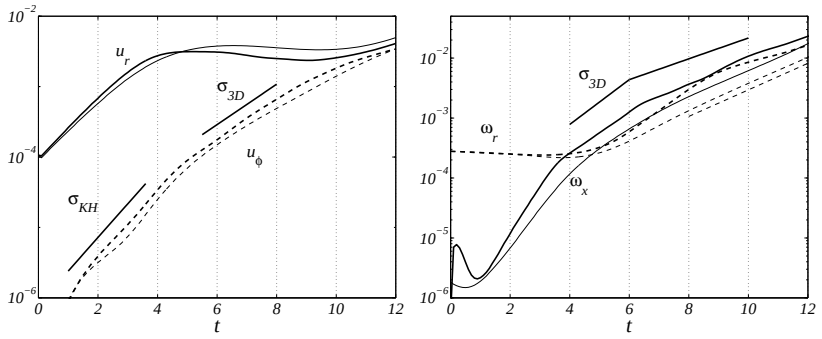

Figure 23: Left : Mean squared radial (u_r solid lines) and azimuthal (u_ϕ dashed lines) velocities of the corrugated low-density jet with $s = 1/3$ (thick lines) and the passive scalar jet (light lines). Right : streamwise (ω_x solid lines) and radial (ω_r dashed lines) enstrophy components.

similar to the one defined by equation (12) and the axial pertubation is found by linear stability analysis on the same Strouhal number $S_t = R/\lambda_x = 0.4$ as in the two-dimensional case. The corrugation is obtained by a radial displacement of the radius of the inflection point of the base flow, say $r(\phi)$, in every point similar to the one used in Brancher, Chomaz & Huerre (1994) :

$$r(\phi) = R\,[1 + 0.05\cos(k_a\,\phi)] \tag{15}$$

For consistency reasons with the configuration of Brancher, the azimuthal wave number is set at $k_a = 3$ which is found to be the selected mode when the homogeneous temporal jet is submitted to a white-noise azimuthal perturbation. A passive-scalar jet and a low-density with $s = 1/3$ jets are simulated at $\mathcal{R}_e = U_s\,D/\nu = 1900$ and $\mathcal{R}_{e\theta} = U_s\,\theta/\nu = 170$. The time scale is $\tau = R/U_s$.

The mean quadratic velocities in the radial and azimuthal directions are measured on figure 23 (left). It is seen that both jets experience a primary mode saturation at $t \approx 6$ and similar growth rates of the Kelvin Helmholtz instability (though higher in the light jet case). The time period between $t = 5$ and $t = 8$ corresponds to a linear growing of three-dimensional modes associated with non-zero azimuthal velocities (radial velocities are also associated with two-dimensional modes). The growth of the azimuthal kinetic energy is slightly higher for the low-density jet. The marked amplification slope gives $\sigma_{3D} = 0.66$ for the light jet and $\sigma_{3D} = 0.56$ gives the best fit for the passive jet.

A significative difference is also observed on the enstrophy components relative to the three-dimensional activity in the jet. It is given on figure 23 (right). From $t = 4$ the low-density jet exhibits a much higher increase of streamwise and radial vorticity compared to the long range amplification of the three-dimensional modes in the passice scalar jet (slope in dashed line). At distinct times, both the streamwise and radial enstrophies experience a sudden decrease of their growth rates preventing them to reach much higher levels. Coarsen res-

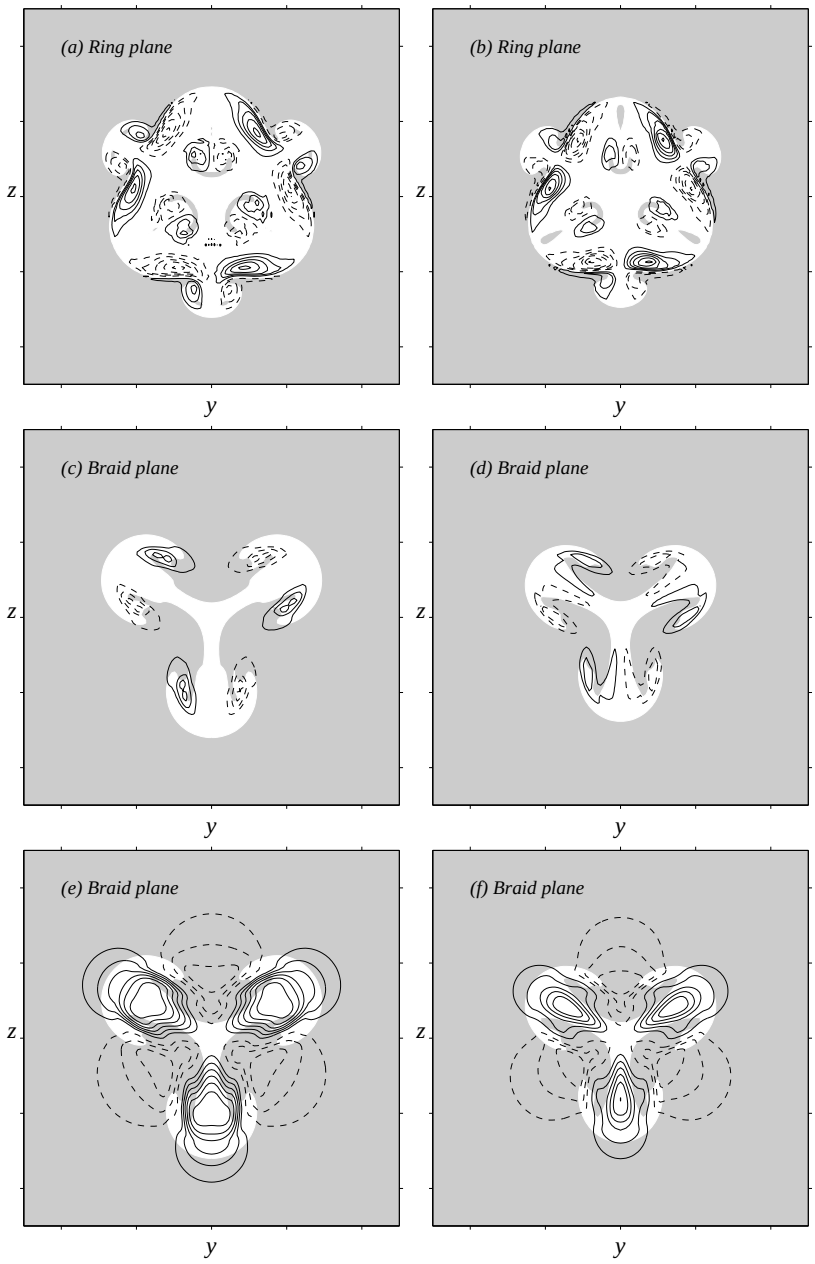

Figure 24: (a) to (d) : cross sections of the streamwise vorticity at $t = 12\tau$, contours increment is $1/\tau$ and the shaded area correspond to heavy fluid above the mean density $\rho_{\text{jet}} + \rho_s/2$. Views (a) and (c) are the ring and braid planes of the passive scalar jet, (b) and (d) are the ring and braid planes of the low density jet with $s = 1/3$. Views (e) and (f) are the radial velocity fields correponding to vorticity field (b) and (d), contour increment is $U_s/20$.

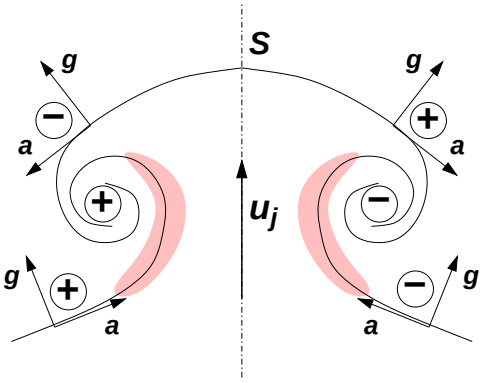

Figure 25: Sketch of the baroclinic contribution on a low-density mushroom structure possibly generated by streamwise ribs in the braid region of variable density mixing-layer or a light jet. The density gradient **g** points upward and the acceleration **a** is oriented according to the advection away from symmetry planes and toward the streamwise rib. The shaded area are baroclinically enhanced vorticity layers promoting the induction of the centerline velocity u_j.

olutions of the low-density jet allow to argue that due to the baroclinic torque redistribution of enstrophy toward higher wave numbers, the diffusive effects are damping the growth of three-dimensional mode sooner in the low-density jet then in the standard one. However it is confirmed that the higher strain rates observed at the saturation time on the two-dimensional simulations are favouring the intensity of the streamwise and radial components of the vorticity field. Higher Reynolds numbers are needed to extend the influence of a full baroclinic vorticity source later in time.

In figure 24 the late development of both flows are compared. Though the strong influence of viscous diffusion at that time, several observations can be put forward. Far after the primary mode saturation, the extra strain rates observed on the centerline of the two-dimensional low-density jets do not seem to enhance the strengh of streamwise vortices in the braid region. Note that the streamwise ribs are not located on the centerline, at least during the rollup of the fundamental mode. The pinching of the jet due to the pairing process may be favorable to the stretching of streamwise vortices by forcing them toward the centerline.

The extensional strain field of the baroclinically modified vortex ring is not the only difference between the homogeneous and the light jet. The baroclinic torque has also a streamwise component that redistributes vorticity in the crosswise planes. On figure 25 the sketch of the baroclinic sources and sinks is given on a streamwise view of an outward mushroom structure resulting from a rib-pair induction on a low-density jet. It is seen that streamwise vortices are supplied by a baroclinic source on the shaded region near the symetry plane $\boldsymbol{S}$.

The Biot-Savart induced radial velocity u_j benefits directly from that vorticity enhancement near the symmetry plane, just as the centerline velocity of the two-dimensional jet on figure 22. This mechanism acts also at the enhancement of the acceleration, and its associated strain field, in the entrainment region below the mushroom pattern. Thus, a divergent sequence where the baroclinically enhanced acceleration feeds back the baroclinic torque in the shaded region of increasing vorticity, may be a valuable scenario for the occurence of spontaneous radial ejection on the braid of light jets. The stability of a pair of counter-rotating vortices in the variable-density braid region is being examined as in Lin & Corcos (1984) to answer if this divergent mechanism exhibits the very high amplification rates associated with side jets.

References

Andreassen, O., Hvidsten, P.O., Fritts, D.C. & Arendt, S. (1998) Vorticity dynamics in a breaking internal gravity wave. Part 1. Initial instability evolution. *J. Fluid Mech.*, **367**:27–46.

Bernal, L.P. & Roshko, A. (1986) Streamwise vortex structure in plane mixing layers. *J. Fluid Mech.*, **170**:499–525.

Borée, J. (2000) Behaviour of highly accelerated variable-density turbulent flows. Application to mixing preparation in internal combustion engines. *Int. Conf. on Variable Density Turbulent Flows,Banyuls,France*, pages 141–152.

Brancher, P., Chomaz, J.M. & Huerre, P. (1994) Direct numerical simulations of round jets: Vortex induction and side jets. *Phys. FLuids*, **6**(5):1768–1774.

Brancher, P. (1996) *Etude numérique des instabilités secondaires de jets.* PhD thesis, Ecole Polytechnique. Laboratoire d'Hydrodynamique.

Brown, G.L. & Roshko, A. (1974) On density effects and large structure in turbulent mixing layers. *J. Fluid Mech.* **64**, *775.*

Bury, Y. (2000) *Structure de jets légers ou lourds en écoulement externe fortement pulsé.* PhD thesis, INPT n^o 1694.

Chapin, V.G., Malandra, M. & Chassaing, P. (1999) A new control strategy of the mixing in two-dimensional jets. *AIAA Paper, 99-3407.*

Chassaing, P., Harran, G. & Joly, L. (1994) Density fluctuation correlations in free turbulent binary mixing. *J. Fluid Mech.* **279**, *239–278.*

Corcos, G.M. & Lin, S.J. (1984) The mixing layer : deterministic models of a turbulent flow. Part 2. The origin of the three-dimensional motion. *J. Fluid Mech.*, **139**:67–95.

Corcos, G.M. & Sherman, F.S. (1976) Vorticity concentration and the dynamics of unstable free shear layers. *J. Fluid Mech.*, **73**:241–264.

Corcos, G.M. & Sherman, F.S. (1984) The mixing layer : deterministic models of a turbulent flow. Part 1. Introduction and the two-dimensional flow. *J. Fluid Mech.*, **139**:29–65.

Corrsin, S. & Uberoi, M.S. (1949) Further experiments on the flow and heat transfer in a heated turbulent air jet. *NACA TN 1865.*

Cortesi, A.B., Yadigaroglu, G. & Banerjee, S. (1998) Numerical investigation of the formation of three-dimensional structures in stably-stratified mixing layers. *Phys. FLuids*, **10**(6):1449–1473.

Crow, S.C. & Champagne, F.H. (1971) Orderly structure in jet turbulence. *J. Fluid Mech.*, **48**:547–591.

Davey, R.F. & Roshko, A. (1972) The two-dimensional mixing region. *J. Fluid Mech.*, **53**:523–543.

Dimotakis, P.E. (1986) Two-dimensional shear-layer entrainment. *AIAA J.*, **24**:1791.

Dritschel, D.G., Haynes, P.H., Juckes, M.N. & Sheperd, T.G. (1991) The stability of a two-dimensional vorticity filament under uniform strain. *J. Fluid Mech.*, **230**:647–665.

Grinstein, F.F., Oran, E.S. & Boris, J.P. (1991) Pressure field, feedback and global instabilitie of subsonic spatially developing mixing layers. *Phys. FLuids A*, **3**(10):2401–2409.

Hermouche, R. (1996) *Etude exprimentale des champs statistiques et des spectres de la zone proche d'un jet Helium-Air.* PhD thesis, INPT.

Huerre, P. & Monkewitz, P.A. (1990) Local and global instabilities in spatially developing flows. *Annu. Rev. Fluid Mech.*, **22**:473–537.

Klaassen, G.P. & Peltier, W.R. (1991) The influence of stratification on secondary instability in free shear layers. *J. Fluid Mech.*, **227**:71–106.

Knio, O.M. & Ghoniem, A. (1991) Three-dimensional vortex simulation of rollup and entrainment in a shear layer. *J. Comp. Phys.*, **97**:172.

Knio, O. & Ghoniem, A. (1992) The three-dimensionnal structure layers under non-symmetric conditions. *J. Fluid Mech.*, **243**:353–392.

Kyle, D.M. & Sreenivasan, K.R. (1993) The instability and breakdown of a round variable-density jet. *J. Fluid Mech.*, **249**:619–664.

Landau, L. & Lifchitz, E. (1989) *Physique théorique.* MIR, Moscou, 2nd edition.

Lele, S. (1989). Direct numerical simulation of compressible free shear flows. Technical Report N89-22827, Center for Turbulence Research.

Lin, S.J. & Corcos, G.M. (1984) The mixing layer : deterministic models of a turbulent flow. Part 3. The effect of plane strain on the dynamics of streamwise vortices. *J. Fluid Mech.*, **141**:139–178.

List, E.J. (1982) Tubulent jets and plumes. *Annual Review of Fluid Mech.*, **14**:189–212.

Martin, J.E. & Meiburg, E. (1991) Numerical investigation of three-dimensionally evolving jets subject to axisymmetric and azimuthal perturbations. *J. Fluid Mech.*, **230**:271–318.

Maslowe, S.A. & Kelly, R.E. (1971) Inviscid instability of an unbounded heterogeneous shear layer. *J. Fluid Mech.*, **48**:405–415.

Michalke, A. (1984) Survey on jet instability theory. *Prog. Aerospace Sci.*, **21**:159–199.

Monkewitz, P.A. & Pfizenmaier, E. (1991) Mixing by side jets in strongly forced and self-excited round jets. *Phys. FLuids A*, **3**(5):1356–1361.

Monkewitz, P.A. & Sohn, K.D. (1988) Absolute instabilities in hot jets. *AIAA J.*, **26**:911–916.

Monkewitz, P.A., Bechert, D.W., Barsikow, B. & Lehmann, B. (1990) Self-excited oscillations and mixing in a heated round jet. *J. Fluid Mech.*, **213**:611–639.

Panchapakesan, N.R. & Lumley, J.L. (1993) Turbulence measurements in axisymmetric jets of air and helium I. and II. *J. Fluid Mech.* **246**, *197.*

Pierrehumbert, R.T. & Widnall, S.E. (1982) The two- and three-dimensional instabilities of a spatially periodic mixing layer. *J. Fluid Mech.*, **114**:59–82.

Raynal, L., Harion, J.-L., Favre-Marinet, M. & Binder, G. (1996) The oscillatory instability of plane variable density jets. *Phys. FLuids*, **8**(4):993–1006.

Reinaud, J., Joly, L. & Chassaing, P. (1999) The baroclinic instability of the two-dimensional shear layer. *TSFP-1, Santa-Barbara*, page 727.

Reinaud, J., Joly, L. & Chassaing, P. (2000) The baroclinic secondary instability of the two-dimensional shear layer. *Phys. FLuids*, **12**(10):2489–2505.

Reinaud, J. (2000) *Analyse physique par simulations numériques lagrangiennes de couches de mélange à densité variable.* PhD thesis, INPT n^o 1689.

Richards, C.D. & Pitts, W.M. (1993) Global density effects on the self-preservation behaviour of turbulent free jets. *J. Fluid Mech.* **254**, *417.*

Rogers, M.M. & Moser, R.D. (1992) The three-dimensional evolution of a plane mixing layer : the Kelvin-Helmholtz rollup. *J. Fluid Mech.*, **243**:183–226.

Sarkar, S. & Pantano, C. (2000) Effects of density variations in compressible turbulent shear flows. *Int. Conf. on Variable Density Turbulent Flows, Banyuls,France*, page 109.

Sarkar, S. (1992) The pressure-dilatation correlation in compressible flows. *Phys. Fluids A* **4**, *2674–2682.*

Schowalter, D.G., Van Atta, C.W. & Lasheras, J.C. (1994) A study of streamwise vortex structure in a stratified shear layer. *J. Fluid Mech.*, **281**:247–292.

S.K.Lele (1994) Compressibility effects on turbulence. *Ann. Rev. Fluid Mech.*, **26**:211–254.

Soteriou, M.C. & Ghoniem, A.F. (1995) Effects of the free-stream density ratio on free and forced spatially developing shear layers. *Phys. Fluids A*, **7**(8):2036.

Staquet, C. (1995) Two-dimensional secondary instabilities in a strongly stratified shear layer. *J. Fluid Mech.*, **296**:73–126.

Thorpe, S.A. (1968) A method of producing a shear flow in a stratified fluid. *J. Fluid Mech.*, **32**:693–704.

Turner, J.S. (1973) *Buoyancy Effects in Fluids.* Cambridge University Press, Cambridge, 2nd edition.

Vreman, A.W., Sandham, N.D. & Luo, K.H. (1996) Compressible mixing layer growth rate and turbulence characteristics. *J. Fluid Mech.*, **46**:235–258.

Zeman, O. (1990) Dilatation dissipation: The concept and application in modeling compressible mixing layers. *Phys. Fluids A* **2**, *178.*